

Transfer Learning for Rapid Extraction of Thickness from Optical Spectra of Semiconductor Thin Films

Siyu Isaac Parker Tian^{1,2}, Zekun Ren^{1,2,†}, Selvaraj Venkataraj², Yuanhang Cheng^{2,‡}, Daniil Bash³, Felipe Oviedo^{4,§}, J. Senthilnath⁵, Vijila Chellappan³, Yee-Fun Lim^{3,6}, Armin G. Aberle², Benjamin P MacLeod⁷, Fraser G. L. Parlange⁷, Curtis P. Berlinguette⁷, Qianxiao Li⁸, Tonio Buonassisi^{1,4,*}, Zhe Liu^{1,4,*,‡}

¹ Low Energy Electronic Systems (LEES), Singapore-MIT Alliance for Research and Technology (SMART), 1 Create Way, Singapore 138602, Singapore

² Solar Energy Research Institute of Singapore (SERIS), National University of Singapore, 7 Engineering Drive, Singapore 117574, Singapore

³ Institute of Materials Research and Engineering (IMRE), Agency for Science, Technology and Research (A*STAR), 2 Fusionopolis Way, Singapore 138634, Singapore

⁴ Department of Mechanical Engineering, Massachusetts Institute of Technology (MIT), 77 Massachusetts Ave., Cambridge, MA 02139, USA

⁵ Institute for Infocomm Research (I2R), Agency for Science, Technology and Research (A*STAR), 1 Fusionopolis Way, Singapore 138632, Singapore

⁶ Institute of Sustainability for Chemicals, Energy and Environment, Agency for Science, Technology and Research (A*STAR), 1 Pesek Rd, Singapore 627833, Singapore

⁷ Department of Chemistry, The University of British Columbia (UBC), 2036 Main Mall, Vancouver, BC V6T 1Z1, Canada

⁸ Department of Mathematics, National University of Singapore (NUS), 21 Lower Kent Ridge Rd, Singapore 119077, Singapore

[†] Now at: Xinterra, Singapore, 77 Robinson Road, Singapore 068896, Singapore

[‡] Now at: Department of Materials Science and Engineering, City University of Hong Kong, Kowloon, Hong Kong, 999077, P.R. China

[§] Now at: Microsoft AI for Good, Redmond, WA 98052, USA

[‡] Now at: School of Materials Science and Engineering, Northwestern Polytechnical University, Xi'an, Shaanxi, 710072, P.R. China

* Corresponding authors: T.B. (buonassi@mit.edu) and Z.L. (zhe.liu@nwpu.edu.cn)

Abstract

High-throughput experimentation with autonomous workflows, increasingly used for the screening and optimization of opto-electronic thin films, requires matching throughput of downstream characterizations. Despite being essential, film thickness' characterization lags in throughput. Although optical spectroscopic methods, *e.g.*, spectrophotometry, provide quick measurements, a critical bottleneck is the ensuing manual fitting of optical oscillation models to the measured reflection and transmission. In this study, we present a machine-learning (ML) framework called *thicknessML*, which rapidly extracts film thickness from spectroscopic reflection and transmission. *thicknessML* leverages transfer learning to generalize to materials of different underlying optical oscillator models (*i.e.*, different material classes). We demonstrate that *thicknessML* can extract film thickness from six perovskite samples in a two-stage process: 1) pre-training on a generic simulated dataset of Tauc-Lorentz oscillator, and 2)

transfer learning to a simulated perovskite dataset of several literature perovskite refractive indices. Results show a pre-training thickness mean absolute percentage error (MAPE) of 5–7%, and an experimental thickness MAPE of 6–19%.

I. Introduction

The rapid advances in machine learning (ML) and robotic automation have enabled autonomous experimental workflow for synthesis, screening, and optimization of new materials in R&D laboratories [1]–[10]. Among the successful applications of high-throughput experimentation (HTE), screening and optimization of function thin-film material is one of the key topics in the recent studies [11]–[13]. In these HTE cases, fabrication of a thin film is shortened to around ten minutes; thus, downstream characterization techniques must match this elevated throughput, either through direct measurements or proxy-variable inference. To accelerate data analysis and information extraction, ML algorithms is adopted for those rapid non-destructive characterization techniques [14]–[16].

Film thickness is among the most essential and yet challenging parameters to measure in high-throughput fashion [17]–[22]. Measuring film thickness is essential because it is an indicator of process control and is necessary in the calculation of some intrinsic materials properties, *e.g.*, conductivity from sheet resistance measurement. Measuring film thickness is challenging in an HTE setting because available methods tend to be either slow or inaccurate. Direct contact-based methods, *e.g.*, cross-sectional scanning electron microscopy (SEM) and profilometry, are destructive and slow. Indirect optical methods, *e.g.*, spectroscopic ellipsometry and transmission-reflection spectrophotometry, are often preferred because of their potential for high throughput, but their accuracy rely on the fitting of optical models, which is based on the knowledge of optical constants of the materials. This knowledge is often not fully available for newly discovered materials, and much experience and trial-and-error are often necessary to build a reliable optical model. For example, lead-halide perovskite thin films typically require a model fitting of 5 – 7 Tauc-Lorentz oscillators (*i.e.*, 15 – 28 fitting parameters) [23].

The knowledge gap and the tedious model-building process motivate us to develop a rapid ML-based analysis method for the optical spectra of semiconductor thin films. Recently, a few studies have reported on thickness characterization using ML [24]–[27]. In Ref. [25], [26], thickness of semiconductor thin films is predicted directly from manufacturing process conditions using ML models without including any characterization as input. Choi and Hong included additional in-situ optical emission spectroscopy sensor data as input [27]. The studies all assumed a time-invariant process-thickness correlation. Using a characterization input, Greco *et al.* [24] applied an artificial neural networks to extract organic semiconductor thin film thickness (ranging from 2 to 30 nm) from X-ray reflectivity (XRR) data. Trained on simulated XRR curves, the neural network achieves 8–18% mean absolute percentage error (MAPE) on simulated and in-line experimental test data.

In this study, to aim for a high-throughput characterization framework, characterization (input) to thickness (output), we tailor our input to the high-throughput and widely accessible characterization, unpolarized optical spectrophotometry in the ultraviolet-visible-near-infrared (UV-Vis-NIR) range (also referred to as UV-Vis); we propose a generalized ML framework, named *thicknessML*, extracting thickness d , optionally with wavelength(λ)-resolved refractive index n (real) and k (imaginary) from spectrophotometry, reflectance $R(\lambda)$ and transmittance $T(\lambda)$. A bottleneck of a generalized ML framework naturally occurs, and is exacerbated in materials discovery, which is the lack of training data. To overcome this bottleneck, we combine numerical simulation and transfer learning as a workflow to generate sufficient data

for a generic case (pre-training) and extend to other cases with minimal amount of data (transfer learning/retraining). We demonstrate the generalized applicability of this two-stage transfer learning workflow of *thicknessML* across different semiconductor material classes (metal oxides to perovskites): I) pre-train the model on a simulated dataset of a single Tauc-Lorentz oscillator (typical for metal oxides). II) minimally retrain the model on a perovskite dataset simulated from a few refractive indices from scientific literature. We then evaluate the retrained model with six experimental perovskite films and attain 6–19% MAPE using only eight literature perovskite $n(\lambda)$, and $k(\lambda)$ spectra as retraining data.

We select the generic case to be where $n(\lambda)$, and $k(\lambda)$ are governed by a simple yet widely used underlying oscillator in semiconductors, Tauc-Lorentz (TL) oscillator [28]. The pre-training learns the mapping from $R(\lambda)$, and $T(\lambda)$ to d , TL-oscillator-governed $n(\lambda)$, and $k(\lambda)$. From physics’ point of view, the learnt mapping is transfer-matrix method (TMM) in an inverse manner under the data bias toward an underlying TL oscillator. The retraining is to transfer the physics in the learnt mapping, while updating the data bias to follow the target material class, *i.e.*, toward underlying oscillators of perovskite refractive indices in our case.

thicknessML, with this transfer learning workflow, can potentially be implemented to any material class when there are a few literature or experimentally fitted refractive indices of that class (for retraining). The term “*thicknessML*” has both specific and general definitions, depending on context. Specifically, it refers to the ML model that outputs thickness (and refractive index) from optical R and T data. Generally, it encompasses the whole of the thickness extraction method, including UV-Vis operation. In this manuscript, we also use the terms “thickness extraction” and “thickness prediction” interchangeably.

II. Results and Discussion

A. Preparation of Simulated Tauc-Lorentz (TL) and Perovskite Datasets

In UV-Vis, estimating thickness relies on fitting underlying oscillator models, which describes the interaction between the impinging electromagnetic wave and electrons within the thin film. Specifically, an oscillator model parameterizes the complex wavelength-resolved refractive index $\tilde{n}(\lambda) = n(\lambda) + ik(\lambda)$ via a middleman, the dielectric function, which, with film thickness d , determines the optical responses $R(\lambda)$ and $T(\lambda)$. Reflecting the variety of materials and their electron densities of states, there are many types of oscillator models, including Tauc-Lorentz, Cauchy, and Drude, among others [29]–[31]. The TL oscillator, widely used for modeling metal oxides, is a default go-to for modeling materials with band gaps, serving as an indispensable building block for semiconductor optical models. Thus, we choose a single TL oscillator to simulate our pre-training dataset. For the retraining perovskite dataset, without explicit simulating $n(\lambda)$, and $k(\lambda)$ with assumed optical models, we turn to experimentally fitted ones in literature.

Two steps are warranted for both datasets: 1) procuring refractive indices $n(\lambda)$ and $k(\lambda)$ via simulation (TL dataset) or literature (perovskite dataset); 2) procuring optical responses $R(\lambda)$ and $T(\lambda)$ based on the obtained $n(\lambda)$, $k(\lambda)$ and specified d via simulation (TMM, for both datasets).

For step 1, in the TL dataset we simulated 1,116 $n(\lambda)$, $k(\lambda)$ spectra by sampling a grid of parameter values (for A , C , E_0 , E_g , with a fixed $\epsilon_\infty=1$) in a Python implementation of a single TL oscillator with λ ranging from 350 to 1000 nm. The λ range is chosen to be a common subset of frequent ranges in UV-Vis measurements and reported literature. In the perovskite dataset we found 18 $n(\lambda)$, $k(\lambda)$ spectra from literature [23], [32]–[35].

For step 2, in both datasets, we simulated $R(\lambda)$, $T(\lambda)$ from obtained $n(\lambda)$, $k(\lambda)$ by specifying a certain number of thicknesses per $n(\lambda)$, $k(\lambda)$ in the range of 10–2010 nm using a Python implementation of TMM [36]. Without loss of generality, we adopt 0° incident angle, and 1 mm glass substrate in the TMM simulation.

B. *thicknessML: convolutional neural network (CNN) and multitask learning (MTL)*

The whole framework of *thicknessML* is shown in Figure 1. For *thicknessML*, we propose a CNN architecture [37]–[39]. CNNs are originally developed for image processing and can capture local spatial information (neighboring pixels) as well as correlation among channels, such as RGB as channels. We use a CNN here to capture R , and T segments at contiguous wavelengths, and thus capture some spatial features like hills and valleys of $R(\lambda)$ and $T(\lambda)$, which are closely related to thickness d . We also concatenate R , and T channel-wise to capture the correlation between R , and T in accordance with the Kramers–Kronig relations in physics [40].

We also propose an MTL architecture. MTL is concurrent learning of multiple tasks, and if the tasks are related, the multiple tasks can help the learning to be more accurate, and less likely to overfit to a specific task (in other word, more generalized learning) [41], [42]. *thicknessML*, in essence, is learning an inverse mapping of TMM; thus, naturally, predicting $n(\lambda)$, and $k(\lambda)$, is highly related to d prediction. Consequently, we concurrently learn to predict d as our main task, and n , k as auxiliary tasks. We also implement a single task learning (STL) architecture (predicting d only), directly satisfying our goal—thickness extraction, for comparison.

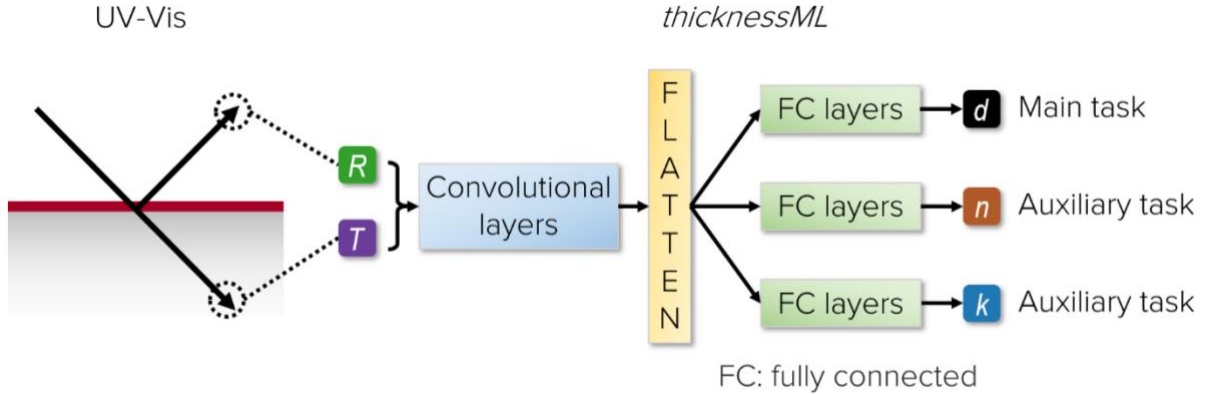


Figure 1. *thicknessML* framework: *thicknessML* receives the $R(\lambda)$, and $T(\lambda)$ spectra and outputs d (and $n(\lambda)$, $k(\lambda)$) for Single Task Learning (MultiTask Learning). Input R , and T spectra first go through four convolutional and max pooling layers for feature extractions, and then get flattened to be passed to three fully connected (FC) and dropout layers, where mapping from extracted features to task targets are drawn. The three dedicated FC-layer blocks for d , $n(\lambda)$, and $k(\lambda)$ corresponds to MTL implementation. STL implementation has the same architecture without the two FC-layer branches for $n(\lambda)$, and $k(\lambda)$. (The adopted incident angle in the UV-Vis is 0° . The inclined beams are drawn to achieve better visual clarity.) The detailed hyperparameters is recorded in S1 section of Supplementary Information.

C. Stage I: Pre-training on the simulated TL dataset

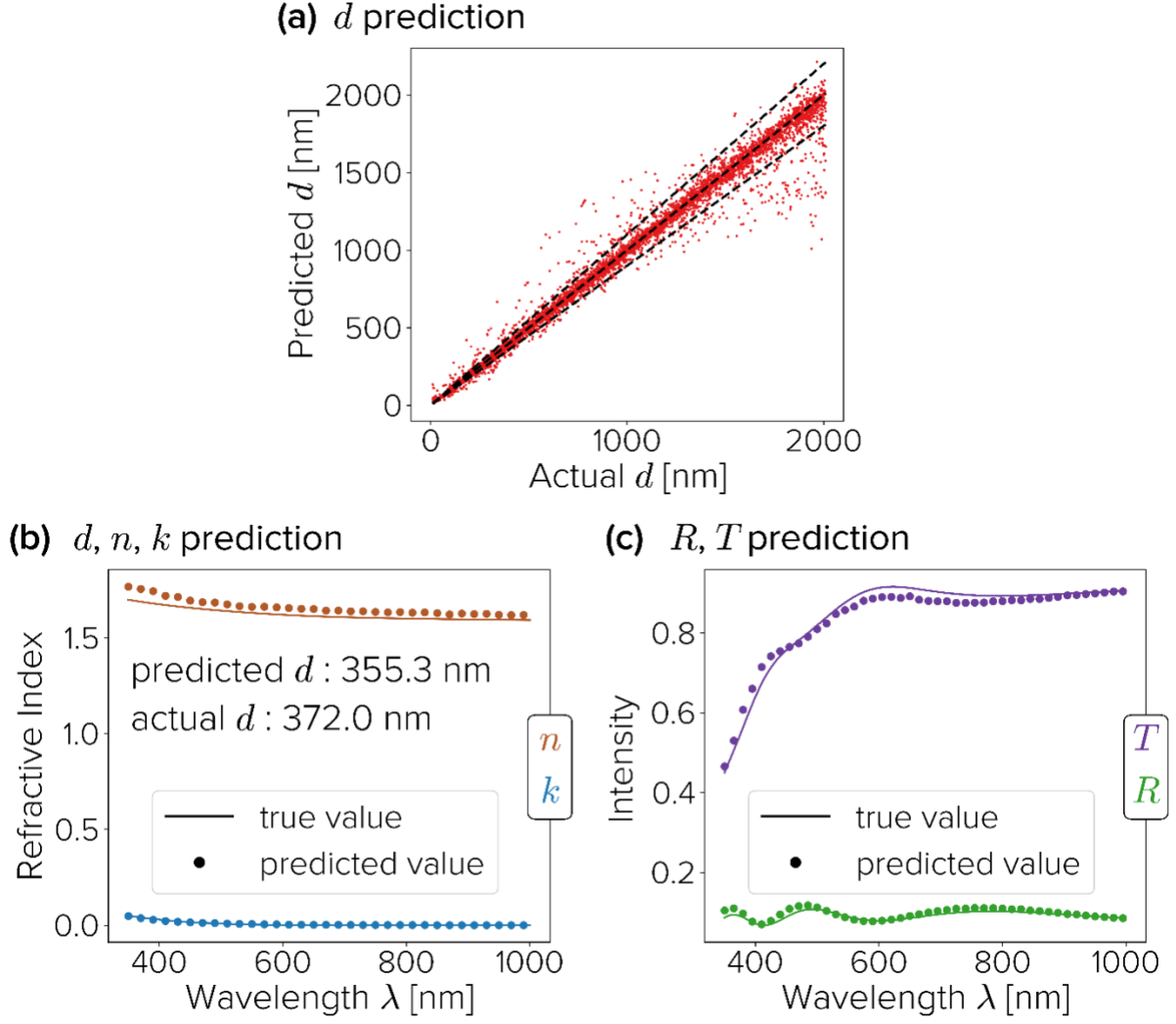


Figure 2. Performance of *thicknessML* (MTL) on the test set (the best run out of three ensemble runs) **a** Predicted d vs. actual d , where the diagonal line indicates perfect prediction, and the two side lines $\pm 10\%$ deviation. **b** d , n , k prediction of an arbitrary sample, where dots denote predictions, and lines actual values. (Dots of 5 nm λ increment are plotted for better visual clarity when predictions are with 1 nm increment as the actual n , k spectra.) **c** R , T reconstruction from predicted d , n , k using TMM on top of actual input R , T spectra, where dots denote predictions, and lines actual values.

Table 1. Performance comparison of *thicknessML* (averaged of three ensemble runs)

	d (<10% deviation)	n (<10% deviation)	k (<10% deviation)
STL	89.6%		
MTL	86.9%	97.5%	44.4%

We split the 1,116 n , k spectra of the TL dataset into 702, 302, and 112 for training, validation and test set respectively. Then we randomly choose 10 thicknesses per pair of n , k spectra in the training and validation set, and 50 thicknesses per pair in the test set to obtain corresponding R , T spectra in the training, validation and test set. The larger number of d per pair of n , k spectra in the test set gives a more stringent thus reliable evaluation of how well *thicknessML* behaves. Three different splits are performed to procure training, validation, and test set for three ensemble runs, and the randomly selected thicknesses for the same n , k spectra are also different in the three splits.

Results of *thicknessML* (MTL) on simulated TL dataset (the best run out of the three ensemble runs) are shown in Figure 2 to illustrate the criteria used for performance evaluation. Three different train-validation-test splits with respect to n , k spectra are carried out for both STL and MTL. The results from the best performing MTL run (in terms of thickness) are selected and shown in Figure 2. Comparison of performances of STL and MTL is documented in Table 1, where the performances are averaged across three ensemble runs.

The criterion adopted stands out most perceptibly in d prediction in Figure 2a, where we quantify the percentage of predictions falling within 10% deviations from the actual values, *i.e.*, the proportion of the points falling within the two side diagonal lines denoting 10% deviation from perfect predictions. Similar criteria pervade through the n , k prediction evaluation in MTL: since n , and k are wavelength-resolved, the within-10%-deviation criterion is quantified across wavelengths on average. For instance, in Figure 2b n and k predictions denoted by the dots should on average across wavelengths fall within 10% from the actual n , k spectra denoted by lines.

Table 1 summarizes the performances. For d prediction, STL achieves 89.6% accuracy (5% MAPE), and MTL 86.9% (7% MAPE). STL slightly better than MTL, seemingly contradict our perception that MTL promotes more generalized learning and better accuracy. This result brings forth a trade-off between a generalized learning and a task-specific learning: a generalized learning may improve the performance through learning more generalized features of the input, but also may negatively impact the performance by dissipating learning capacity into various tasks (thus losing focus on the intended main task). However, with transfer learning to follow, the generalized learning of MTL has an edge compared to the task-specific STL. Accuracies reach 97.5% and 44.4% for n and k prediction respectively in MTL. We notice the relatively poor performance of k prediction, and we attribute it to several reasons:

- Many k values on larger wavelengths are near or at zero, *e.g.*, on the magnitude of 10^{-2} . This renders the percentage-based within-10%-deviation criterion unduly stringent. A different choice of absolute-error-based criterion may reflect the k prediction performance more appropriately.
- The many near-zero and at-zero k values bias the output data distribution heavily and unfavorably.
- The prediction of wavelength-resolved values is naturally harder than the prediction of a scalar value.

Nevertheless, we acknowledge the k prediction limitation of *thicknessML*, and caution potential users to place more confidence in d prediction than n , k prediction, as the inclusion of auxiliary tasks (n , k prediction) is to help the main task, d prediction.

D. Stage II: Transfer learning to the simulated perovskite dataset, and verify on six experimental perovskite thin films

Transfer learning takes the pre-trained model (a warm start from the pre-trained weights instead of random initializations) and let the partial or full weights continue to train on a new dataset (retraining). Through the pre-trained weights, transfer learning [43] allows knowledge learnt in the pre-trained task to be transferred to a related new task with much less data and training. In our case, the pre-trained weights carry the knowledge of an inverse mapping of TMM, from R , and T to d , n , and k , and the retraining further adapts the mapping to a dataset whose underlying oscillator models are of perovskite materials.

We propose and run two types of transfer learning: (1) full-weight retraining, to continue updating the weights for both convolutional and fully connected layers. (2) partial-weight

retraining, to freeze the weights for convolutional layers, responsible for feature extraction, while updating the fully connected layers. To provide a baseline, we also implemented a case of learning from scratch (from random initialized weights as in pre-training).

Dataset preparation for transfer learning and learning from scratch is different because learning from scratch typically requires much more data (as in the pre-training) than transfer learning. Different train-test-split ratios of the perovskite dataset, containing 18 perovskite n , and k from literature, are executed to evaluate the transfer learning performance. No validation set is employed in transfer learning. The number of d per n , k spectra for training and test sets still follow the TL dataset convention, 10 for training set and 50 for test set. In terms of learning from scratch, we evaluate one case, a 13–5 train-test split (for number of n , k spectra), and assigned 500 d per n , k spectra for training while maintaining the 50 d per n , k spectra for test. The extremely large number of assigned d per n , k spectra is to complement the small number of n , k spectra available, ensuring enough training data in learning from scratch.

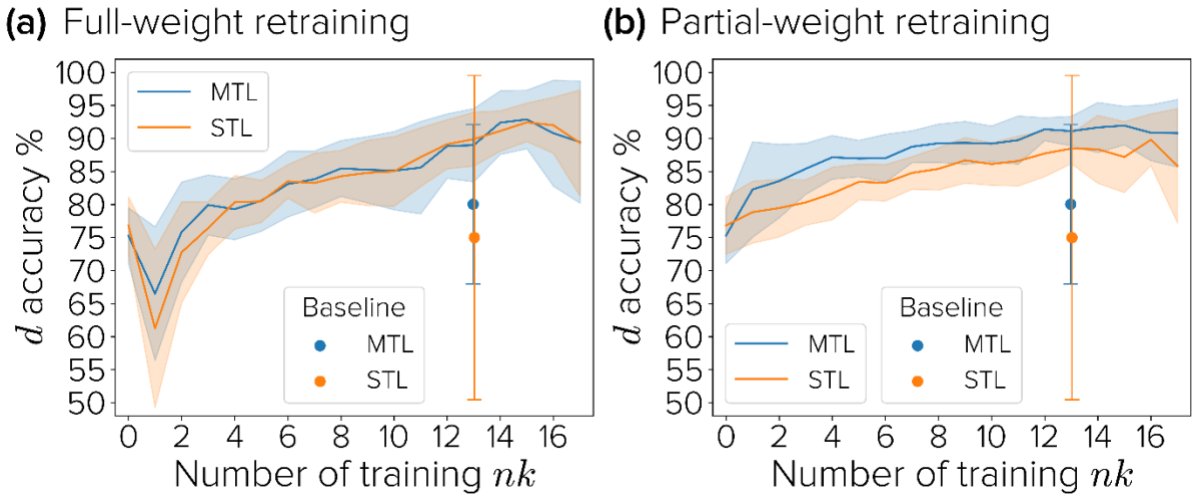


Figure 3. d accuracy (evaluated on test set) vs. number of retraining n , k spectra (out of a total of 18) **a** Full-weight retraining, where every weight is updated during retraining. **B** Partial-weight retraining, where weights in the convolutional layers are frozen, and only the weights in fully connected layers are updated. Bands denote transfer learning using the corresponding number of retraining n , k spectra with 10 d per n , k spectra; solid lines and spreads denote the mean, and the standard deviation of runs from 5 different train-test splits and an ensemble of three pre-trained *thicknessML* models; dots with error bars denote a case of learning from scratch on 13 n , k spectra with 500 d per n , k spectra, while the dot and the error bar denote the mean, and the standard deviation of runs from 5 different train-test splits.

Figure 3 shows the transfer learning results compared with learning from scratch, on the simulated perovskite dataset, and offers several observations. First, partial-weight retraining behaves better when the number of retraining n , k spectra is small (≤ 12). Full-weight retraining performs better when the number of retraining n , k spectra is large (> 12). Full-weight retraining experiences a decrease in accuracy first, then followed by an eventual increase. Compared to partial-weight retraining, full-weight retraining has more weights to update, and thus is more flexible. Flexibility has both pros and cons: when the number of retraining n , k data is small, flexibility more easily steers *thicknessML* away from optimal weights (an initial drop in accuracy); when the number of retraining n , k spectra becomes large enough, flexibility offers a higher learning capacity, and thus a better accuracy. Second, transfer learning has a much smaller spread (standard deviation of d accuracies from ensemble runs), *i.e.*, much stabler performance than learning from scratch. Although able to exceed the performance of transfer learning in certain runs, learning from scratch seems to be largely affected by specific train-

test splits. Transfer learning also requires much less data compared to learning from scratch (10 d per n, k spectra vs. 500 d per n, k spectra). Third, STL almost rivals MTL in both kinds of transfer learning, while MTL has higher accuracy in the case of partial-weight retraining. The higher accuracy in the case of partial-weight retraining reflects the feature learnt by MTL being more generalized, thus conducive to transfer learning.

To validate this transfer learning framework of *thicknessML*, we evaluate its performance on experimental perovskite films. We deposit six methylammonium lead iodide (MAPbI₃) films with assorted precursor solution concentrations and spin coating speeds. We perform UV-Vis and profilometry measurements and compare with the *thicknessML* predictions in Figure 4. Pre-trained *thicknessML* is retrained on the simulated perovskite dataset with eight retraining n, k spectra using a partial-weight retraining. The choice of eight perovskites is deliberate to be more distinct from MAPbI₃ by not containing methylammonium (MA). The resulting predictions have a 6–19% MAPE.

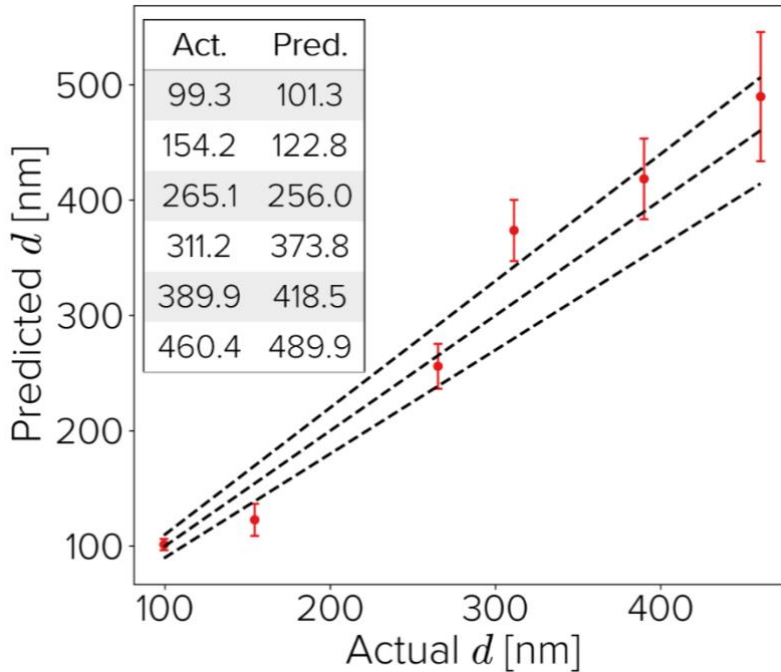


Figure 4. *thicknessML*-predicted thickness vs. profilometry-measured thickness of six perovskite films. The inset lists the actual (Act.) measured and predicted (Pred.) thicknesses of the films (mean values for predicted thickness). The error bar on the predicted thickness denotes the standard deviation of various runs of the ensemble *thicknessML*, while the dot the mean. The diagonal line plots the perfect prediction, and the two side lines $\pm 10\%$ deviation.

To evaluate *thicknessML* as a high-throughput characterization framework, we also record its throughput. The bulk of time per sample is spent on UV-Vis, and depends on specific tools, where the prediction of one film only adds about 0.4 ms. In this study, UV-Vis is measured by a stand-alone tool with an integrating sphere and takes about 2 minutes per sample to measure $R(\lambda)$, and $T(\lambda)$ of 0° incident angle. The one-off retraining (transfer learning) of *thicknessML* takes a few minutes, and the one-off pre-training takes about 3.3 hours on a desktop equipped with Intel(R) Core(TM) i7-4790 CPU and NVIDIA GeForce GTX 1650 GPU.

III. Conclusions

Materials discovery requires characterization throughputs that match those of experimental synthesis. While an increasing number of platforms offer high-throughput thin-film synthesis,

available film-thickness characterization tools have limitations. The indirect optical measurement, UV-Vis, although high-throughput, needs optical model fitting to obtain thickness, requiring expertise and extensive human time. Thus, we propose a characterization framework *thicknessML* that is:

- high-throughput (enabled by machine learning), able to automatically extract thickness within seconds from UV-Vis measurements of semiconductor films without optical model fitting.
- generalized with minimal amount of data (enabled by transfer learning), able to step across different material classes (materials typically possessing the same or similar underlying oscillator models, such as metal oxides) with a few literature/experimentally fitted n , k of the target material class.

thicknessML achieves its generalization through a two-stage process—1) pre-training a generic model on a generic TL dataset, and 2) transferring to (retraining on) a specific material class. We demonstrate the two-stage process of *thicknessML* on six experimental (MAPbI₃) films, achieving 6–19% MAPE on the predicted film thicknesses.

While further research may yield models with even better thickness prediction accuracy, we believe that this study opens a new direction of leveraging transfer learning in automatic thickness extraction and serves as an inspiration for future research in the area of high-throughput characterization.

IV. Methods

Refractive Index Simulation from single Tauc-Lorentz Oscillator

The Python implementation of the single Tauc-Lorentz oscillator entails the implementation of the following equations [29]:

$$n = \sqrt{\frac{1}{2}(\sqrt{\varepsilon_r^2 + \varepsilon_i^2} + \varepsilon_r)} \quad (1)$$

$$k = \sqrt{\frac{1}{2}(\sqrt{\varepsilon_r^2 + \varepsilon_i^2} - \varepsilon_r)} \quad (2)$$

$$E = \frac{hc}{\lambda} \quad (3)$$

$$\varepsilon_i(E) = \begin{cases} \frac{1}{E} \frac{AE_0C(E-E_g)^2}{(E^2-E_0^2)^2+C^2E^2}, & \text{for } E > E_g \\ 0, & \text{for } E \leq E_g \end{cases} \quad (4)$$

$$\begin{aligned} \varepsilon_r(E) = \varepsilon_\infty + \frac{A \cdot C \cdot a_{ln}}{2 \cdot \pi \cdot \zeta^4 \cdot a \cdot E_0} \cdot \ln \left[\frac{E_0^2 + E_g^2 + \alpha E_g}{E_0^2 + E_g^2 - \alpha E_g} \right] - \frac{A}{\pi \cdot \zeta^4} \frac{a_{atan}}{E_0} \left[\pi - \operatorname{atan} \left(\frac{2E_g + \alpha}{c} \right) \right. \\ \left. + \operatorname{atan} \left(\frac{-2E_g + \alpha}{c} \right) \right] + 2 \frac{AE_0C}{\pi \zeta^4} \left\{ E_g (E^2 - \gamma^2) \left[\pi + 2 \operatorname{atan} \left(\frac{\gamma^2 - E_g^2}{\alpha c} \right) \right] \right\} \\ - 2 \frac{AE_0C}{\pi \zeta^4} \frac{E^2 + E_g^2}{E} \ln \left(\frac{|E - E_g|}{E + E_g} \right) + 2 \frac{AE_0C}{\pi \zeta^4} E_g \ln \left[\frac{|E - E_g|(E + E_g)}{\sqrt{(E^2 - E_0^2)^2 + E_g^2 C^2}} \right] \end{aligned} \quad (5)$$

where h , and c are Planck's constant and speed of light, and

$$a_{ln} = (E_g^2 - E_0^2)E^2 + E_g^2C^2 - E_0^2(E_0^2 + 3E_g^2),$$

$$a_{atan} = (E^2 - E_0^2)(E_0^2 + E_g^2) + E_g^2C^2,$$

$$\zeta^4 = (E^2 - \gamma^2)^2 + \frac{\alpha^2 C^2}{4},$$

$$\alpha = \sqrt{4E_0^2 - C^2},$$

$$\gamma = \sqrt{E_0^2 - C^2/2},$$

After combining all the above equations, $n(\lambda)$ and $k(\lambda)$ are parameterized by five fitting parameters, A , C , E_0 , E_g , and ε_∞ . We fix $\varepsilon_\infty = 0$, and sample grids for each parameter as follows— A , 10 to 200 with 11 grid nodes; C , 0.5 to 10 with 10 grid nodes; E_0 , 1 to 10 with 10 grid nodes, and E_g , 1 to 5 with 10 grid nodes. After sampling, we randomly select 1,116 n , k spectra to be our dataset.

Transfer-Matrix Method Simulation

The Python implementation of TMM simulation follows the equations in [36], assuming no roughness, and fully coherent layers. The incident angle is 0° , and the incident medium above the films and the exit medium below the glass substrate are air (with infinite thickness). The glass substrate with a thickness of 1 mm corresponds to the actual substrate used in depositing the six MAPbI₃ films. The incident angle around 0° for transmission and 8° for reflectance is also used in the UV-Vis measurement due to the setup of the integrating sphere. The small discrepancy of incidence angles between measurement and simulation only causes negligible difference in reflectance spectra.

Convolutional Neural Network

Designed for image recognition, the classic CNN architecture consists of three main types of layers: convolutional, pooling and fully connected. Convolutional layers connect with input and each other through local filters of fixed sizes and extract the features within the filter window through convolution. In the convolutional layer, information from local pixels (within the filter window), or the local feature, gets concentrated and to be passed as a single pixel to the next layer. With the addition of each convolutional layer, features extracted are of higher and higher level (features that are more global). Thus, the series of convolutional layers becomes a feature extractor, containing features ranging from low level to high. A pooling layer usually follows convolutional layers, to downsample the spatial dimensions of the given input. Max pooling (retaining the maximum values during downsampling) has widest usage, which aims to retain the most salient features. Fully connected layers are exactly a multilayer perceptron (MLP), taking the extracted features as input. The name “fully connected” arises from the comparison with convolutional layers, which are locally connected through filters. An MLP is a universal approximator [44] for mappings between input and output, and serves to learn the mapping from extracted features to the output. In addition to the three types of layers, *thicknessML* also adds dropout layers after fully connected layers to prevent overfitting. The detailed layers and hyperparameter of *thicknessML* can be found in section S1 of Supplementary Information.

Section S2 of Supplementary Information peeks into the black box of *thicknessML*, and visualizes activation maps of an example R , T spectra (from TL dataset). The four rows of activation maps correspond to the outputs of the four convolutional layers (after ReLU activation) respectively (ten filters are randomly chosen for each convolutional layer to produce

the activation maps). Certain filters activate maximally at peaks or valleys of the R , T spectra, which closely relates to film thickness.

Multitask Learning

Multitask learning is concurrent learning of multiple tasks, while each task can be a regression or classification task as in supervised learning. This concurrent learning is achieved by parameter sharing, which can be implemented via hard (using the same parameters) or soft (using similar parameters) parameter sharing. Ruder provides a helpful overview of multitask learning in [41]. *thicknessML* adopts the hard parameter sharing, letting the prediction of d , n , and k share the same parameters of convolutional layers, *i.e.*, the same feature extractor. The shared feature extractor promotes extraction of more generalized features, and the auxiliary tasks also provide regularization by introducing an inductive bias. The three tasks of d , n , and k prediction retain individual fully connected layer blocks to individually process and map the extracted features to respective values.

Transfer Learning

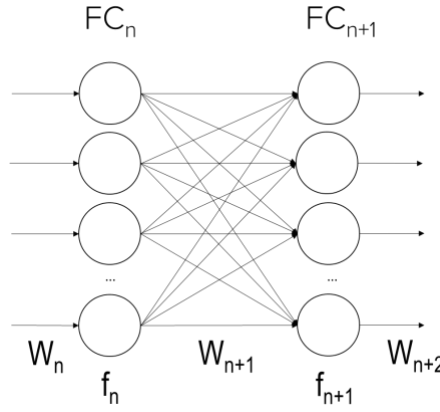


Figure 5. A simplified neuron representation of fully connected layer n and $n+1$, where W_n denotes the weights associated with layer n , and f_n the activation functions.

Figure 5 depicts a simplified representation of certain fully connected layers with associated weights and activation functions. Weights are to perform weighted sum with incoming inputs from previous layers, and activation functions are to decide whether to activate with a hard or soft cut-off based on the weighted sum. The convolutional layers follow the same principle except the incoming inputs are spatially arranged, and the weights are in the spatial form of filters. During the pre-training, and learning from scratch of *thicknessML*, the weights are randomly initialized, and the weights are updated through training data via backpropagation. The knowledge of an inverse mapping of TMM of an underlying TL oscillator is embedded in the trained weights of the pre-trained *thicknessML*. This knowledge via the pre-trained weights is then transferred to the perovskite dataset in two manners—continue to update only the weights of the fully connected layers (partial-weight retraining), or weights of both the convolutional layers and the fully connected layers (full-weight retraining).

MAPbI₃ Film Deposition, UV-Vis Measurement, and Profilometry Measurement

In the deposition of MAPbI₃, six combinations of two thickness-affecting process variables, concentration of the perovskite precursor solution (PbI₂ and MAI with molar ratio of 1:1), and spin coating speed, are used and recorded in Table 2. The deposited films are then measured

for UV-Vis with an Agilent Cary 7000 UV-Vis-NIR Spectrophotometer, and for profilometry with a KLA Tencor P-16 + Plus Stylus Profiler.

Table 2. Values of concentration of precursor solution and spin coating speed used in the deposition of MAPbI₃ films, and measured and predicted thickness of the films (as recorded in Figure 4).

Film No.	Concentration of Precursor Solution (M)	Spin Coating Speed (rpm)	Measured Thickness (nm)	Predicted Thickness (nm)
1	0.5	3000	154.17	122.8
2	0.5	6000	99.29	101.3
3	1.25	3000	389.89	418.5
4	1.25	6000	265.07	256.0
5	1.5	3000	460.35	489.9
6	1.5	6000	311.15	373.8

Data Availability

Datasets used in this study is provided in <https://github.com/PV-Lab/thicknessML>.

Code Availability

Code for pre-training, and transfer learning is provided, together with pre-trained *thicknessML* models, in <https://github.com/PV-Lab/thicknessML>.

Acknowledgements

We acknowledge financial support from the National Research Foundation (NRF) Singapore through the Singapore Massachusetts Institute of Technology (MIT) Alliance for Research and Technology's Low Energy Electronic Systems research program, and the Energy Innovation Research Program (grant number, NRF2015EWT-EIRP003-004 and NRF-CRP14-2014-03 and Solar CRP: S18-1176-SCRP), TOTAL SA research grant funded through MITEI, the Accelerated Materials Development for Manufacturing Program at A*STAR via the AME Programmatic Fund by the Agency for Science, Technology and Research under Grant No. A1898b0043, and Solar Energy Research Institute of Singapore (SERIS), a research institute at the National University of Singapore (NUS) supported by the National University of Singapore (NUS), the National Research Foundation Singapore (NRF), the Energy Market Authority of Singapore (EMA), and the Singapore Economic Development Board (EDB). C.P.B., B.P.M., and F.G.L.P. are grateful to the Canadian Natural Science and Engineering Research Council (RGPIN-2018-06748) and Natural Resources Canada's Energy Innovation Program (EIP2-MAT-001) for financial support.

Author Contribution

Conceptualization, B.P.M., F.G.L.P., F.O., C.P.B. and T.B.; Methodology, Z.L., S.I.P.T., Z.R., T.B., Q.L., Y.F.L., J.S., F.O., B.P.M. and F.G.L.P.; Software, Z.L. and S.I.P.T.; Investigation, S.V., Y.C., D.B., V.C., and S.I.P.T.; Writing – Original Draft, S.I.P.T., and Z.L.; Writing – Review & Editing, Z.L., T.B. and S.I.P.T.; Funding Acquisition, T.B. and A.G.A.; Resources, A.G.A.; Supervision, Z.L., T.B., and Q.L.

Competing interests

Although our laboratory has IP filed covering photovoltaic technologies and materials informatics broadly, we do not envision a direct COI with this study, the content of which is open sourced. Three of the authors (Z.R., T.B., Z.L.) own equity in Xinterra Pte Ltd, which applies machine learning to accelerate novel materials development.

References

- [1] B. A. Rizkin, A. S. Shkolnik, N. J. Ferraro, and R. L. Hartman, “Combining automated microfluidic experimentation with machine learning for efficient polymerization design,” *Nat. Mach. Intell.*, vol. 2, no. 4, pp. 200–209, Apr. 2020, doi: 10.1038/s42256-020-0166-5.
- [2] B. Burger, P. M. Maffettone, V. V Gusev, *et al.*, “A mobile robotic chemist,” *Nature*, vol. 583, no. 7815, pp. 237–241, 2020, doi: 10.1038/s41586-020-2442-2.
- [3] K. Abdel-Latif, F. Bateni, S. Crouse, and M. Abolhasani, “Flow Synthesis of Metal Halide Perovskite Quantum Dots: From Rapid Parameter Space Mapping to AI-Guided Modular Manufacturing,” *Matter*, vol. 3, no. 4. Cell Press, pp. 1053–1086, Oct. 2020. doi: 10.1016/j.matt.2020.07.024.
- [4] F. Häse, L. M. Roch, C. Kreisbeck, and A. Aspuru-Guzik, “Phoenix: A Bayesian Optimizer for Chemistry,” *ACS Cent. Sci.*, vol. 4, no. 9, pp. 1134–1145, 2018, doi: 10.1021/acscentsci.8b00307.
- [5] F. Mekki-Berrada, Z. Ren, T. Huang, *et al.*, “Two-step machine learning enables optimized nanoparticle synthesis,” *npj Comput. Mater.*, vol. 7, no. 1, p. 55, Dec. 2021, doi: 10.1038/s41524-021-00520-w.
- [6] P. F. Newhouse, D. Guevarra, M. Umehara, *et al.*, “Combinatorial alloying improves bismuth vanadate photoanodes: Via reduced monoclinic distortion,” *Energy Environ. Sci.*, vol. 11, no. 9, pp. 2444–2457, Sep. 2018, doi: 10.1039/c8ee00179k.
- [7] S. Ament, M. Amsler, D. R. Sutherland, *et al.*, “Autonomous materials synthesis via hierarchical active learning of nonequilibrium phase diagrams,” *Sci. Adv.*, vol. 7, no. 51, p. 4930, Dec. 2021, doi: 10.1126/sciadv.abg4930.
- [8] Z. Liu, N. Rolston, A. C. Flick, T. W. Colburn, Z. Ren, R. H. Dauskardt, and T. Buonassisi, “Machine learning with knowledge constraints for process optimization of open-air perovskite solar cell manufacturing,” *Joule*, vol. 6, no. 4, pp. 834–849, Apr. 2022, doi: 10.1016/j.joule.2022.03.003.
- [9] B. P. MacLeod, F. G. L. Parlane, A. K. Brown, J. E. Hein, and C. P. Berlinguette, “Flexible automation accelerates materials discovery,” *Nature Materials*. 2021. doi: 10.1038/s41563-021-01156-3.
- [10] A. E. Gongora, B. Xu, W. Perry, C. Okoye, P. Riley, K. G. Reyes, E. F. Morgan, and K. A. Brown, “A Bayesian experimental autonomous researcher for mechanical design,” *Sci. Adv.*, vol. 6, no. 15, p. eaaz1708, Apr. 2020, doi: 10.1126/sciadv.aaz1708.
- [11] B. P. MacLeod, F. G. L. Parlane, T. D. Morrissey, *et al.*, “Self-driving laboratory for accelerated discovery of thin-film materials,” *Sci. Adv.*, vol. 6, no. 20, p. eaaz8867, 2020, doi: 10.1126/sciadv.aaz8867.
- [12] X. Du, L. Lüer, T. Heumueller, *et al.*, “Elucidating the Full Potential of OPV Materials Utilizing a High-Throughput Robot-Based Platform and Machine Learning,” *Joule*, vol. 5, no. 2, pp. 495–506, Feb. 2021, doi: 10.1016/J.JOULE.2020.12.013.
- [13] D. Bash, Y. Cai, V. Chellappan, *et al.*, “Multi-Fidelity High-Throughput Optimization of Electrical Conductivity in P3HT-CNT Composites,” *Adv. Funct. Mater.*, vol. 31, no. 36, p. 2102606, Sep. 2021, doi: 10.1002/adfm.202102606.
- [14] F. Oviedo, Z. Ren, S. Sun, *et al.*, “Fast and interpretable classification of small X-ray diffraction datasets using data augmentation and deep neural networks,” *npj Comput.*

- Mater.*, vol. 5, no. 1, 2019, doi: 10.1038/s41524-019-0196-x.
- [15] N. Taherimakhsoosi, B. P. MacLeod, F. G. L. Parlange, T. D. Morrissey, E. P. Booker, K. E. Dettelbach, and C. P. Berlinguette, "Quantifying defects in thin films using machine vision," *npj Comput. Mater.*, vol. 6, no. 1, 2020, doi: 10.1038/s41524-020-00380-w.
 - [16] Z. Liu, F. Oviedo, E. M. Sachs, and T. Buonassisi, "Detecting Microcracks in Photovoltaics Silicon Wafers using Variational Autoencoder," in *Conference Record of the IEEE Photovoltaic Specialists Conference*, Jun. 2020, vol. 2020-June, pp. 0139–0142. doi: 10.1109/PVSC45281.2020.9300366.
 - [17] T. D. Lee and A. U. Ebong, "A review of thin film solar cell technologies and challenges," *Renew. Sustain. Energy Rev.*, vol. 70, pp. 1286–1297, Apr. 2017, doi: 10.1016/J.RSER.2016.12.028.
 - [18] M. Powalla, S. Paetel, E. Ahlswede, R. Wuerz, C. D. Wessendorf, and T. Magorian Friedlmeier, "Thin-film solar cells exceeding 22% solar cell efficiency: An overview on CdTe-, Cu(In,Ga)Se₂-, and perovskite-based materials," *Appl. Phys. Rev.*, vol. 5, no. 4, p. 041602, Dec. 2018, doi: 10.1063/1.5061809.
 - [19] C. Mackin, A. Fasoli, M. Xue, Y. Lin, A. Adebisi, L. Bozano, and T. Palacios, "Chemical sensor systems based on 2D and thin film materials," *2D Mater.*, vol. 7, no. 2, p. 022002, Feb. 2020, doi: 10.1088/2053-1583/AB6E88.
 - [20] J. E. Ellis, S. E. Crawford, and K. J. Kim, "Metal–organic framework thin films as versatile chemical sensing materials," *Mater. Adv.*, vol. 2, no. 19, pp. 6169–6196, Oct. 2021, doi: 10.1039/D1MA00535A.
 - [21] Y. S. Choi, J. W. Kang, D. K. Hwang, and S. J. Park, "Recent advances in ZnO-based light-emitting diodes," *IEEE Trans. Electron Devices*, vol. 57, no. 1, pp. 26–41, Jan. 2010, doi: 10.1109/TED.2009.2033769.
 - [22] X. Chen, Z. Zhou, Y. H. Lin, and C. Nan, "Thermoelectric thin films: Promising strategies and related mechanism on boosting energy conversion performance," *J. Mater.*, vol. 6, no. 3, pp. 494–512, Sep. 2020, doi: 10.1016/J.JMAT.2020.02.008.
 - [23] M. Shirayama, H. Kadowaki, T. Miyadera, *et al.*, "Optical Transitions in Hybrid Perovskite Solar Cells: Ellipsometry, Density Functional Theory, and Quantum Efficiency Analyses for CH₃NH₃PbI₃," *Phys. Rev. Appl.*, 2016, doi: 10.1103/PhysRevApplied.5.014012.
 - [24] A. Greco, V. Starostin, C. Karapanagiotis, A. Hinderhofer, A. Gerlach, L. Pithan, S. Liehr, F. Schreiber, and S. Kowarik, "Fast fitting of reflectivity data of growing thin films using neural networks," *J. Appl. Crystallogr.*, vol. 52, pp. 1342–1347, 2019, doi: 10.1107/S1600576719013311.
 - [25] C.-Y. Shen, Y.-J. Chen, S. T. Wang, C.-Y. Chang, and R.-C. Hwang, "The Estimation of Thin Film Properties by Neural Network," *Autom. Control Intell. Syst.*, vol. 4, no. 2, p. 15, Mar. 2016, doi: 10.11648/j.acis.20160402.12.
 - [26] D. Hwan Kim, J. Eun Choi, T. Min Ha, and S. Jeon Hong, "Modeling with Thin Film Thickness using Machine Learning," 2019.
 - [27] J. E. Choi and S. J. Hong, "Machine learning-based virtual metrology on film thickness in amorphous carbon layer deposition process," *Meas. Sensors*, vol. 16, p. 100046, Aug. 2021, doi: 10.1016/J.MEASEN.2021.100046.

- [28] S. I. P. Tian, Z. Liu, V. Chellappan, *et al.*, “Rapid and Accurate Thin Film Thickness Extraction via UV-Vis and Machine Learning,” in *2020 47th IEEE Photovoltaic Specialists Conference (PVSC)*, 2020, pp. 128–132. doi: 10.1109/PVSC45281.2020.9300634.
- [29] G. E. Jellison and F. A. Modine, “Parameterization of the optical functions of amorphous materials in the interband region,” *Appl. Phys. Lett.*, vol. 69, no. 3, pp. 371–373, 1996, doi: 10.1063/1.118064.
- [30] M. Born and E. Wolf, *Principles of Optics*. Pergamon Press, 1984.
- [31] P. Drude, C. R. Mann, and R. Andrews, *The Theory of Optics*. New York: Longmans, Green, and Co., 1902.
- [32] H. Fujiwara, N. J. Podraza, M. I. Alonso, M. Kato, K. Ghimire, T. Miyadera, and M. Chikamatsu, “Organic-inorganic hybrid perovskite solar cells,” in *Springer Series in Optical Sciences*, vol. 212, Springer, Cham, 2018, pp. 463–507. doi: 10.1007/978-3-319-75377-5_16.
- [33] S. Manzoor, J. Häusele, K. A. Bush, A. F. Palmstrom, J. Carpenter, Z. J. Yu, S. F. Bent, M. D. McGehee, and Z. C. Holman, “Optical modeling of wide-bandgap perovskite and perovskite/silicon tandem solar cells using complex refractive indices for arbitrary-bandgap perovskite absorbers,” *Opt. Express*, vol. 26, no. 21, pp. 27441–27460, Oct. 2018, doi: 10.1364/OE.26.027441.
- [34] J. Werner, G. Nogay, F. Sahli, *et al.*, “Complex Refractive Indices of Cesium-Formamidinium-Based Mixed-Halide Perovskites with Optical Band Gaps from 1.5 to 1.8 eV,” *ACS Energy Lett.*, vol. 3, no. 3, pp. 742–747, Mar. 2018, doi: 10.1021/acsenergylett.8b00089.
- [35] P. Löper, M. Stuckelberger, B. Niesen, *et al.*, “Complex refractive index spectra of CH₃NH₃PbI₃ perovskite thin films determined by spectroscopic ellipsometry and spectrophotometry,” *J. Phys. Chem. Lett.*, vol. 6, no. 1, pp. 66–71, Jan. 2015, doi: 10.1021/jz502471h.
- [36] E. Centurioni, “Generalized matrix method for calculation of internal light energy flux in mixed coherent and incoherent multilayers,” *Appl. Opt.*, vol. 44, no. 35, pp. 7532–7539, 2005, doi: 10.1364/AO.44.007532.
- [37] Y. LeCun, B. Boser, J. S. Denker, D. Henderson, R. E. Howard, W. Hubbard, and L. D. Jackel, “Backpropagation Applied to Handwritten Zip Code Recognition,” *Neural Comput.*, vol. 1, no. 4, pp. 541–551, Dec. 1989, doi: 10.1162/NECO.1989.1.4.541.
- [38] L. Cun, J. Henderson, Y. Le Cun, J. S. Denker, D. Henderson, R. E. Howard, W. Hubbard, and L. D. Jackel, “Handwritten Digit Recognition with a Back-Propagation Network”.
- [39] K. O’shea and R. Nash, “An Introduction to Convolutional Neural Networks”.
- [40] E. Hecht, *Optics*, 5 edition. Pearson, 2016.
- [41] S. Ruder, “An Overview of Multi-Task Learning in Deep Neural Networks,” 2017, Accessed: Jul. 21, 2021. [Online]. Available: <http://sebastianruder.com/multi-task/index>.
- [42] R. CARUANA, “Multitask Learning,” *Mach. Learn.*, vol. 28, pp. 41–75, 1997, doi: 10.1007/978-3-030-01620-3_5.
- [43] K. Weiss, T. M. Khoshgoftaar, and D. D. Wang, “A survey of transfer learning,” *J. Big Data*, vol. 3, no. 1, pp. 1–40, Dec. 2016, doi: 10.1186/S40537-016-0043-6/TABLES/6.

- [44] K. Hornik, M. Stinchcombe, and H. White, “Multilayer feedforward networks are universal approximators,” *Neural Networks*, vol. 2, no. 5, pp. 359–366, Jan. 1989, doi: 10.1016/0893-6080(89)90020-8.

Supplementary Information

S1. *thicknessML* Hyperparameters

Table S1. *thicknessML* hyperparameters in convolutional neural network.

<i>thicknessML</i> Hyperparameters	Setting
Convolutional layers	4
Filter size	[8, 5, 3, 3]
No. of filters	[512, 128, 64, 32]
Max pooling layers	4
Spatial extent of pooling layers	[3,3,2,2]
Number of units for fully connected layers for d	[2048, 1024, 512, 1]
Number of units for fully connected layers for n	[2048, 1024, 651]
Number of units for fully connected layers for k	[2048, 1024, 651]
Dropout rate of fully connected layers	0.3
Epochs	2000
Batch size	128
Optimization algorithm	AdaGrad
Learning rate	0.001 (initial and restored every 50 epochs since 150)

S2. Visualization of *thicknessML* Activation Maps of an Example R , T Spectra

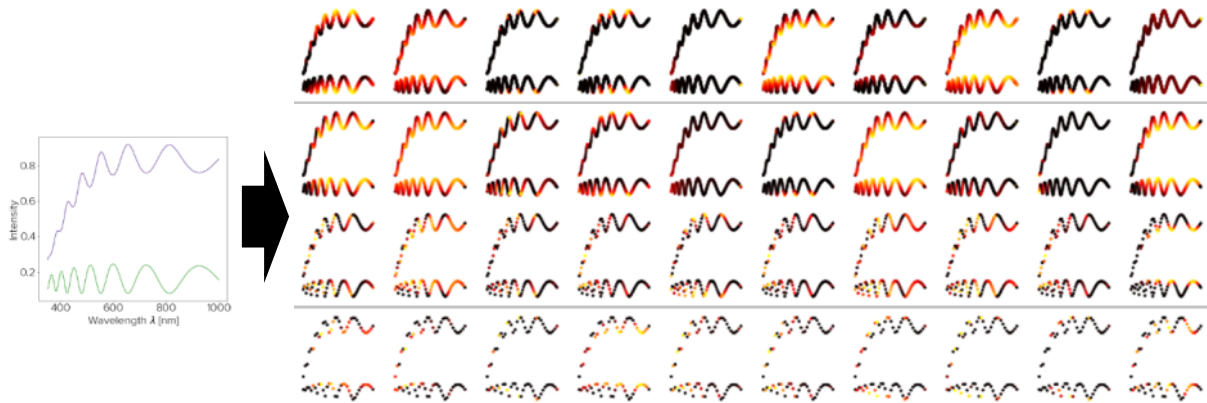


Figure S1. Visualization of activation maps of ten random filters of the 4 convolutional layers (top to bottom: the first to fourth convolutional layer) from a pre-trained *thicknessML*. Lighter color indicates higher activation of the spectra.

Figure S1 plots the activation maps of an example R , T spectra, where an activation map is the output of a given filter (weights of convolutional layers) applied to the previous layer. Activation maps give some intuition into which part of the spectra each filter focuses on (gets more activated). For instance, we can see some filters focus on extracting the hill tops and valley bottoms of the spectra, some filters get activated when encountering certain gradients like uphill or downhill portions, and some filters recognize more holistically where the whole hills and valleys are. This tallies well with the physical

picture, where positions of the hills and valleys are the most prominent feature in the R , T spectra when thickness d is varied. More oscillations (hills and valleys) are being seen with a larger d .